Palaeogeography, Palaeoclimatology, Palaeoecology 581 (2021) 110609

Contents lists available at ScienceDirect

Palaeogeography, Palaeoclimatology, Palaeoecology

journal homepage: www.elsevier.com/locate/palaeo

Miocene East Asia summer monsoon precipitation variability and its possible driving forces

Zhengchuang Hui [a,b,c], Xuewen Zhou [a], Manuel Chevalier [d,e], Xiao Wei [a], Yanfang Pan [a,b,c,*], Yingyong Chen [a,b,c]

[a] College of Geography and Environmental Science, Henan University, Kaifeng 475004, China
[b] National Demonstration Center for Environmental and Planning, Henan University, Kaifeng 475004, China
[c] Key Laboratory of Geospatial Technology for the Middle and Lower Yellow River Regions (Henan University), Ministry of Education, Kaifeng 475004, China
[d] Institute of Geosciences, Sect. Meteorology, Rheinische Friedrich-Wilhelms-Universität Bonn, Auf dem Hügel 20, 53121 Bonn, Germany
[e] University of Lausanne, Institute of Earth Surface Dynamics IDYST, Faculté des Géosciences et l'Environnement, Bâtiment Géopolis, CH-1015 Lausanne, Switzerland

ARTICLE INFO

Editor: Howard Falcon-Lang

Keywords:
Pollen
Tianshui basin
Probability density functions
Quantitative reconstruction

ABSTRACT

The East Asian summer monsoon (EASM) precipitation is vital to hydrology, ecology and societal activities in the densely populated region of East Asia. However, its long-term evolution history and driving forces during the relatively warm Miocene remain unclear, even conflicting in some intervals. Here, we present a new, and quantitative record of EASM precipitation during Miocene using the Bayesian approach of Climate Reconstruction Software (CREST) based on pollen flora from the Tianshui Basin located on the northwestern Tibetan Plateau (TP). The results demonstrate that a strong and relatively stable EASM precipitation period occurred during the Neogene in northern China at ~17.1–13.6 Ma, which was followed by a strong and gradual decreasing period between ~13.6 and 7.4 Ma. This trend was abruptly stopped at ~7.4 Ma with the beginning of a period of large amplitude precipitation increase. The comparison analysis reveals that the gradual decrease of EASM precipitation during the period of ~17.1–7.4 Ma was primarily controlled by the global cooling, whereas the significant increase period after ~7.4 Ma was mainly related to the late Miocene uplift of the TP, supporting climate model simulations, in which both the global temperature and palaeogeography play important roles in regulating the long-term evolution of EASM precipitation.

1. Introduction

The precipitation of the East Asian summer monsoon (EASM) - a key component of the Asian Monsoon - influences almost all aspects of hydrology, ecology and societal activities in East Asia, where roughly one-third of the world's population lives (Webster et al., 1998; Clift and Plumb, 2008; Chen et al., 2015). Research on the evolution of the EASM precipitation and their driving forces has consequently received much research attention from the climatology and Earth science communities (Wang et al., 2019; Clift et al., 2014; Ao et al., 2016; Lu et al., 2019; Ren et al., 2020; Piao et al., 2020; Zhang et al., 2018; Wang et al., 2020; Zhao et al., 2020a; Hui et al., 2020; Miao et al., 2016, Miao et al., 2017; Jiang and Ding, 2008, 2009).

Previous studies based on geochemical proxies from marine sediments in the South China Sea (SCS) show that the EASM intensity exhibited a gradually weakening pattern from the Middle Miocene climate Optimum (~ 17–15 Ma, MMCO) to the end of the Neogene at tectonic time scales (million-year timescales, Wan et al., 2010; Wei et al., 2006; Clift, 2020). These results were partly supported by a sporopollen-based vegetation history during the Neogene from inland Asia that showed similar trends with a gradual decreasing trend of EASM, although the spatial resolution is low (Miao et al., 2016, 2017; Jiang and Ding, 2008, 2009; Zhao et al., 2020b). In contrast, the magnetic parameter and mineral ratios records from Chinese Loess Plateau (CLP) and Qaidam Basin indicate that the intense EASM of the MMCO, gradually weakened during the middle to late Miocene (~ 14–8 Ma), but strengthened again after the late Miocene (~ 8 Ma) (Ren et al., 2020; Sun et al., 2015; Zhao et al., 2020a).

* Correspondimh author at: College of Geography and Environmental Science, National Demonstration Center for Environmental and Planning, Key Laboratory of Geospatial Technology for the Middle and Lower Yellow River Regions (Henan University), Ministry of Education, Henan University, Kaifeng 475004, China.
E-mail addresses: huizhch@henu.edu.cn (Z. Hui), 499210902@qq.com (X. Zhou), chevalier.manuel@gmail.com (M. Chevalier), Weixiao0809@163.com (X. Wei), panyanfang@henu.edu.cn (Y. Pan), chenyy@henu.edu.cn (Y. Chen).

https://doi.org/10.1016/j.palaeo.2021.110609
Received 17 April 2021; Received in revised form 3 August 2021; Accepted 3 August 2021
Available online 9 August 2021

Two dominant hypotheses are currently in use to define the driving forces of the EASM evolution during the Neogene: 1) the "weakening hypothesis" that emphasizes the dominant role of global temperature changes in controlling long term evolution of EASM (Miao et al., 2017; Jiang and Ding, 2008; Zhao et al., 2020a; Wan et al., 2010), and 2) the "fluctuation hypothesis" that underlines the importance of paleogeographic changes (such as Tibetan plateau uplift and Panama seaway closure) (Ren et al., 2020; Sun et al., 2015; Zhao et al., 2020a), as suggested by model simulations (Farnsworth et al., 2019; Zhang et al., 2018). In summary, the evolution process and driving forces of EASM during the Neogene are still controversial, even conflicting in some periods (such as late Miocene). This is partly because long, Neogene quantitative EASM precipitation records are rare in East Asia.

In this study, we used the pollen record from the Tianshui basin in NE Tibetan Plateau (TP) (Hui et al., 2011) as the basis to perform quantitative reconstructions of summer precipitation amount – precipitation during the wettest quarter (PWetQ) – using the software of CREST (Climate Reconstruction Software) and database of GBIF_v2.1.0 developed by Chevalier et al. (2014) and Chevalier (2019) to provide a quantitative record of EASM intensity in the northern China during Miocene. This quantitative record combined with existing records enables us to determine the history of EASM during the Miocene and investigate its driving mechanisms.

2. Regional settings

The Tianshui Basin is situated on the NE Tibetan Plateau (Fig. 1a) and is bounded by the Huajialing Mountain to the northwest, the West Qinling Mountains to the southwest and the Liupan Mountains to the northeast (Fig. 1b). The basin covers a transition zone from humid monsoonal zone to arid zone of northwest of China and to the alpine climate of Tibetan Plateau that is highly sensitive to climate change (Li et al., 1988). At present, the climate in this region is mainly controlled by the East Asian Monsoon, characterized by hot-humid summers and cold-dry winters. The mean annual temperature (MAT) and mean annual precipitation (MAP) of this region are ~10 °C and ~ 500 mm, respectively, with most of the precipitation falling in June to September (PWetQ ~300 mm) (Liu et al., 2016). Geological records indicate that the EASM has been influencing the climate in this studied region since the Miocene (Miao et al., 2016; Sun and Wang, 2005), confirming the Tianshui Basin's potential capacity to capture the variability of the EASM.

3. Materials and methods

3.1. Depositional environments and chronology of the YW section

The studied section - Yanwan (YW) has a thickness of 288 m and is located in the Tianshui Basin, NE TP (Fig. 1b). Based on lithologic properties and depositional characteristics, three depositional environments can be distinguished from bottom to top: Unit 1, ~ 132 m thick - flood plain systems, consists mainly of fine-grained light brown-yellow mudstones intercalated with brown-red mudstones; Unit 2, ~ 128 m thick - lake mudflat with sheet-floods systems, consists mainly of light blown-yellow calciferous mudstones interbedded with browned mudstones with fine laminations; Unit 3, ~ 28 m thick - flood plain/distal fan

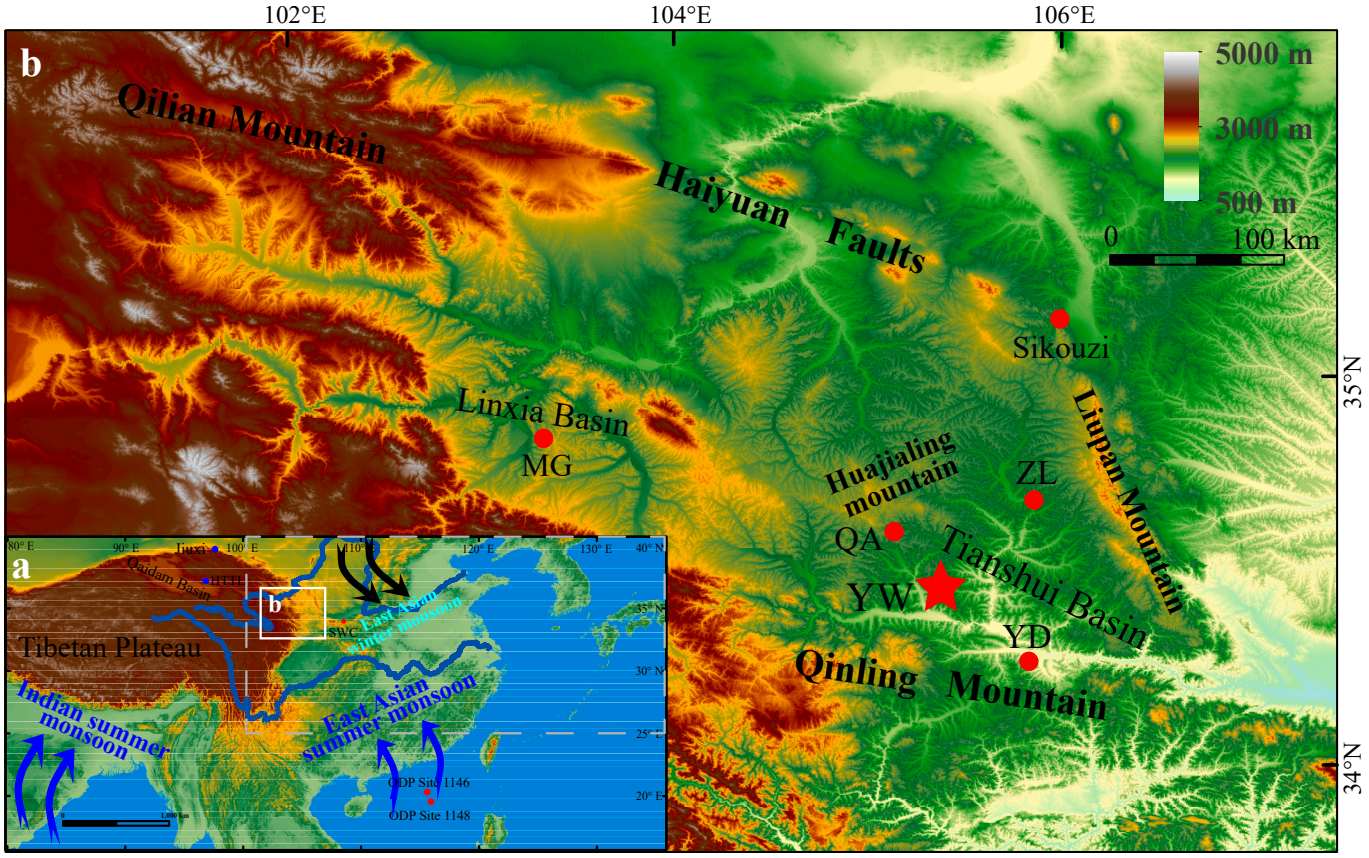

Fig. 1. Geographic setting of YW section. (a) Location and atmospheric circulation patterns of the Tianshui Basin, and other sections mentioned in the text. (b) Geomorphological setting of Tianshui basin, and other mentioned sections in the adjacent basins. The grey dashed rectangle indicates the calibration region. The red star shows the studied section and the red and blue dots show the mentioned sections in the text. YW: Yanwan section, YD: Yaodian section, MG: Maogou section, QA: Qinan, ZL: Zhuanglang core, SWC: Shuiwancun section, HTTL: Huaitoutala section. (For interpretation of the references to colour in this figure legend, the reader is referred to the web version of this article.)

systems, consists of brown-red and brown-yellow mudstones with horizontal bedding and grey-green bands.

The chronology of the Yanwan section is based on both biostratigraphic age control and high resolution magnetostratigraphy. A lot of mammal fossils were discovered in Yanwan section at the depth of 49.5 m and 93.5 m, respectively, including *Hipparion weihoense*, *Acerorhinus fuguensis*, *Chilotherium habereri* and *Chilotherium wimani*, and thus anchor the temporal framework at the early Late Miocene (Deng, 2016). A total of ~1600 paleomagnetic samples were collected at an interval of 0.25 m from YW section. Based on the above mammal fossil age constraints, the measured magnetic polarity sequence of Yanwan section has been compared with the Geomagnetic Polarity Time Scale of Cande and Kent (1995), yielding an age range of 17.1–6.1 Ma for the studied section. More details of the depositional environments and chronology have been reported by Zhang et al. (2013) and Alonso-Zarza et al. (2009).

3.2. Pollen record for the YW section

The pollen record of the YW section includes 114 samples, with average temporal resolution of 96 kyr (Hui et al., 2011). Approximately 80 different palynomorphs were identified at family or genus level from this section (See supplementary materials), and the nearest living relative (NLRs) of these 80 fossil taxa are mainly distributed in the subtropical, temperate and warm-temperate humid monsoon climate area now, such as tree species *Liquidambar*, *Pterocarya*, Rutaceae, *Podocarpus*, *Quercus*, *Ulmus*, *Betula*, *Pinus*, *Juglans*, *Salix*, Cupressaceae and *Fraxinus*, as well as widely distributed shrub and herb species, such as Rosaceae, Poaceae, *Artemisia*, Chenopodiaceae, Amaranthaceae, Caryophyllaceae and Celastraceae. Based on the relative changes in abundances of trees, shrubs and herbs, Hui et al. (2011) concluded that broad-leaved forest dominated the Tianshui Basin during the 17.1–8.5 Ma, which was replaced by steppe vegetation after 8.5 Ma. This succession of vegetation types clearly shows, albeit qualitatively, variations of humidity from the middle Miocene to the late Miocene. We refer the readers to Hui et al. (2011) for more detailed information of the vegetation changes.

3.3. CREST method

To obtain the quantitative records of EASM from the YW section pollen data, the CREST method and software described in Chevalier et al. (2014) and the CREST-formatted GBIF database developed by Chevalier (2019) were used to reconstruct PWetQ. The CREST method is a Bayesian approach that uses modern plant distributions and corresponding climate data to define probability density functions (PDFs) describing the relationship between a unique plant taxon and specific climate variables, such as PWetQ (Chevalier et al., 2014, 2020).

The method was originally developed for Quaternary studies, but its generalist assumptions make it adapted to study older records, providing an adaptation of the terminology. CREST was first presented for pollen data and the estimation of the PDFs worked as follow. The method uses a two-steps approach to define the probabilistic links between climate and pollen taxa (Fig. 2). First simple, parametric PDF are fitted for each plant species composing the pollen taxa (PDF_{sp}) and then these PDF_{sp} are averaged to estimate the response of the pollen-type as a single unit (PDF_{pol}). Here, we do not have pollen taxa but rather fossil taxa, each one associated with an ensemble of modern nearest living relatives. While different in essence, the same modelling concepts can be employed to estimate plausible climate responses. First, we calculate the modern PDFs of the nearest living relatives of our fossil plants, and then we combine them together to estimate the resulting ensemble of possible climate responses.

Finally, climate reconstructions can be estimated using the standard approach, wherein PDF_{pol} are multiplied with weight being derived from the observed abundances. To minimize the effect of different taphonomic processes and/or production rate of different taxa on climate reconstructions (Xu et al., 2005; Li et al., 2011), the percentages for each taxon are normalized by the average of the percentages observed in the fossil sequence (Chevalier et al., 2014, 2020). The multiplication of the different taxon PDF_{pol} results in a posterior distribution, from which the best estimate of a climate parameter and its uncertainties can be obtained.

We acknowledge that the modelling assumptions underlying this work, including the use of modern plant-climate relationships to infer the response of our fossil taxa, are not negligible. However, these form the common basis of all qualitative and quantitative studies of such distant times. Some uncertainties should thus be kept in mind when interpreting the results.

3.4. Taxa selection and definition of the calibration dataset

Eighty taxa were identified in our fossil record. Using such a high number of taxa to reconstruct climate is not recommended and the CREST method often perform better with a set of climate-sensitive taxa are selected. Two main reasons can explain this: 1) the sensitivity of some taxa to PWetQ is weaker than their sensitivity to other environmental parameters and including those could add a bias to the reconstruction because their variability would mainly reflect changes in these unaccounted for parameters (Juggins et al., 2015), or 2) the diversity of

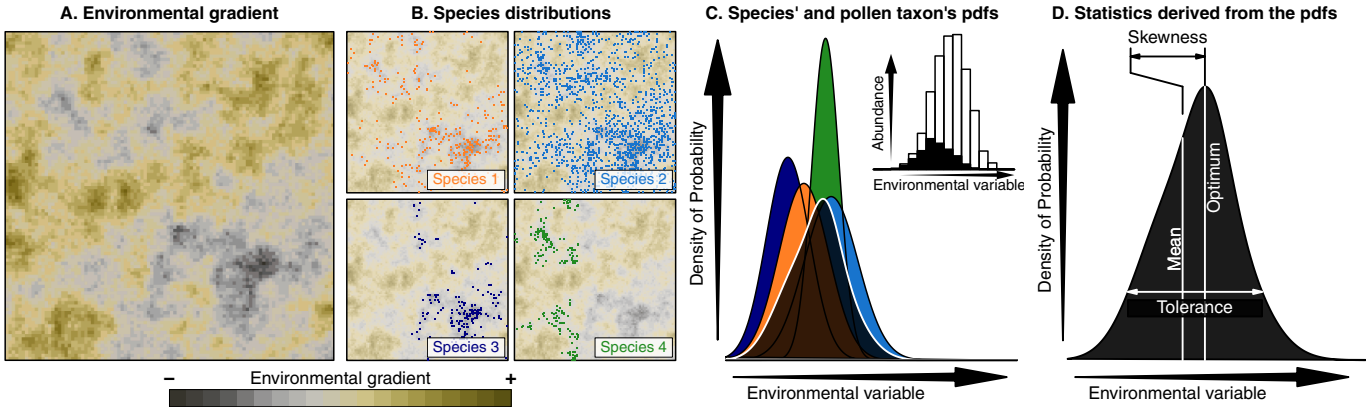

Fig. 2. Conceptual representation of the fitting of probability density functions (pdfs) using randomly generated data. (A) Modern distribution of the environmental variable of interest. (B) Modern distribution of four species producing pollen grains in the environment. (C) Four curves representing four pdfs of the species represented in B. Inset histogram represents distribution of modern environment (white) that is occupied by at least one of the four species of interest (black), highlighting the preference for lower values. (D) Representation of statistics (optimum, mean, and width/uncertainty) that can be measured from each pdf to infer climate preferences and tolerances.

species composing each taxon is too large estimate a reliable and unique climate response, which can lead to a saturation of the signal of the PDFs that end up reflecting the distribution of the modern climate space rather than a specific climate response (Chevalier et al., 2014).

Using the diagnostics tools embedded in the CREST software and the modern correlation between plant distribution and climate gradients, we identified a subset of sensitive taxa to reconstruct PWetQ reconstruction: *Alnus*, *Carpinus*, *Celtis*, *Corylus*, *Fraxinus*, *Ginkgo*, Hamamelidaceae, *Juglans*, *Liquidambar*, Meliaceae, Onagraceae, *Ostryopsis*, *Picea*, *Podocarpus*, *Pterocarya*, *Pteroceltis*, *Rhus*, Rutaceae, *Stellera*, Taxodiaceae, *Tsuga* and *Zelkova*.

Another important step in the reconstruction is the definition of a range for the calibration dataset to estimate reliable PDFs.

To enable the reconstruction of potentially large vegetation and climatic changes, we defined a large rectangular region from 25°N to 40°N, 100°E to 135°E as the calibration dataset, including various climate types (subtropical, warm-temperate and temperate and humid, semi-humid and semi-arid climate types; Fig. 1a). The diversity of the YW pollen floral itself (consisting of tropical, subtropical, warm-temperate and temperate taxa) also supports the definition of such the calibration dataset (Hui et al., 2011).

Finally, we evaluate the influence of each pollen-type used to reconstruct PWetQ reconstructions, by suing the leave-one-out (LOO) cross-validation method proposed in CREST. This approach provides a direct measurement of the relative importance of each pollen taxon by assessing the differences between the reconstruction with all the selected taxa and without the given taxon of interest (Supplementary Fig. S1). Over, *Fraxinus*, *Podocarpus*, *Liquidambar*, *Alnus* and Rutaceae indicate a relative wetter summer and *Ostryopsis*, *Corylus*, *Rhus*, *Picea* and *Juglans* indicate a relative drier summer. However, the classification of a given taxon as wetter or drier is variable, depending on the other taxa recorded in the pollen assemblage. For example, *Celtis* is generally a dry indicator during the period of ~16–17 Ma because the assemblage is composed of many wetter taxa but *Celtis* and becomes a generally wet indicator during the period of ~10–12 Ma because other, drier taxa have replaced the wetter ones (Supplementary Fig. S1).

4. Results

The reconstructed PWetQ indicates that its best estimated values mainly vary between ~700–400 mm (Fig. 3). Overall, these results show a gradual reduction from ~660 mm at ~17.1 Ma to ~400 mm at ~7.4 Ma, and after that precipitation increased sharply to ~650 mm at 6.1 Ma (Fig. 3). The EASM records can be roughly divided into three periods (Fig. 3). During the period of ~17–13.2 Ma, the EASM precipitation shows relatively stable conditions with the maximum average value of ~618 mm (standard deviation $\sigma = 41.5$ mm). From ~13.2 to 7.4 Ma, the EASM precipitation decrease from ~620 mm to ~400 (mean $\sigma = 65.8$ mm), with an aberration interval of ~10–9 Ma (Fig. 3). From ~7.4 Ma, the EASM precipitation increased sharply from the lowest value during the studied period of 377 mm to ~650 mm at ~6.1 Ma (mean $\sigma = 73.4$ mm). It should be noted that the standard deviation for each interval shows gradual increase, implying an increase in changing amplitude.

5. Discussion

5.1. Comparison between the quantitative and qualitative records of EASM

Various types of proxies have been applied to reconstruct the history of the Neogene EASM, mainly including pollen assemblage, magnetic parameters and geochemical indicators (Fig. 4). The pollen assemblages (also including pollen species indicators) from the SWC section (Weihe Basin, Fig. 1a, Zhao et al., 2020a), YD and YW sections (Tianshui Basin, Fig. 1b, Hui et al., 2011; Liu et al., 2016), Sikouzi section (Fig. 1b, Jiang and Ding, 2008), MG section (Linxia Basin, Fig. 1a, Ma et al., 1998), and Jiuxi basin (Fig. 1a, Ma et al., 2005) indicate an in-phase drying pattern from ~17 Ma to 6.1 Ma (Supplementary Fig. S2). The biggest difference between the quantitative reconstructed PWetQ and the pollen assemblage is the trend after 7.4 Ma. The former indicates a trend to increasing wetness whereas the latter show a gradually drying (Fig. 4a and b). This difference may result from the different pollen species used for quantitative reconstruction and qualitative inference. Prior to quantitative reconstruction, all the pollen species' sensitivities to EASM were assessed using the diagnostics tools embedded in the CREST software (Chevalier et al., 2014) and the pollen types that were not directly sensitive to

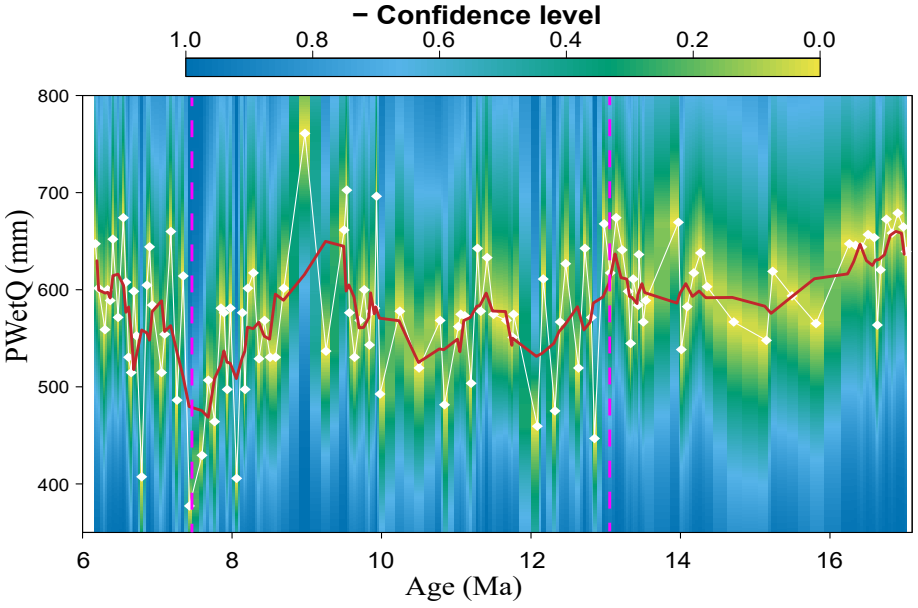

Fig. 3. PWetQ reconstructions from Yanwan section in Tianshui Basin. White diamonds represent reconstructed values and the red line shows the 5-point running average. Yellow to blue background colour gradient represents uncertainties, here expressed as confidence intervals. Purple vertical lines show the different EASM evolution periods boundaries. (For interpretation of the references to colour in this figure legend, the reader is referred to the web version of this article.)

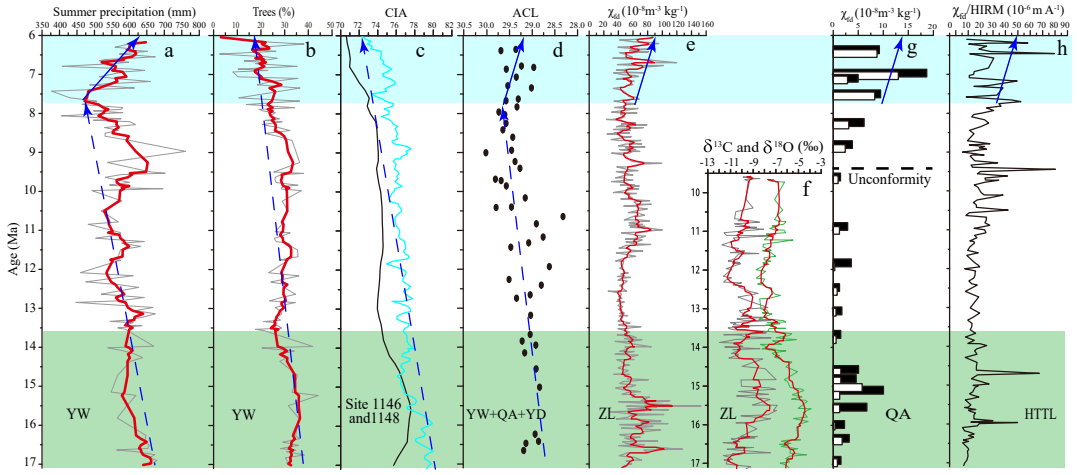

Fig. 4. Comparison of reconstructed summer precipitation, trees pollen abundance percentages, biomarker, geochemical and magnetic proxy records from the Tianshui Basin and Qaidam Basin from ~17.1 to 6.1 Ma. The red lines show the 5-point running average. The blue dashed lines with arrows show the general decreasing trends, whereas the blue solid lines with arrows in light cyan band highlight the strengthening trend. (a) Reconstructed summer precipitation records from the studied YW section in Tianshui Basin. (b) Tree pollen percentages from the studied YW section in Tianshui Basin (Hui et al., 2011). (c) Chemical Index of Alteration (CIA) data from ODP site 1146 (light green) and site 1148 (black) South China Sea (Wan et al., 2010). (d) Proxy of Averaged Chain Length (ACL) records from the YW, YD and QA sections in the Tianshui Basin (Peng et al., 2016). (e) The frequency-dependent magnetic susceptibility records from ZL core in the Tianshui Basin (Qiang et al., 2011). (f) The pedogenic carbon (grey) and oxygen (green) isotope records from ZL core in the Tianshui Basin (Dong et al., 2018). (g) The frequency-dependent magnetic susceptibility records from QA section in the Tianshui Basin (Hao et al., 2008). (h) The χ_{fd}/HIRM records of HTTL section, Qaidam Basin (Nie et al., 2020). Note that there is an unconformity possible resulting from high rainfall erosion at ~9.5 Ma at Qinan (Fig. 5f), such that the high χ_{fd} and χ_{fd}/HIRM values observed from Zhuanglang and HTTL were not recorded at Qinan section. (For interpretation of the references to colour in this figure legend, the reader is referred to the web version of this article.)

PWetQ were excluded from the reconstruction. Generally speaking, the herbs were excluded from the reconstruction since they are widely distributed (also partly because of the low identification resolution of pollen types) and do not convey specific climate parameter information, such as the commonly observed *Artemisia* and Poaceae pollen types in the sediments. Therefore, we propose that the pollen assemblages are composite indicators which may include both the EASM and aridification signal (Hui et al., 2011; Liu et al., 2016; Ma et al., 2005).

The biomarker proxy of Averaged Chain Length (ACL) records from the QA, YD and YW sections in same basin (Tianshui Basin) support our EASM records, which show that the degree of aridity increased from ~17–8 Ma, and decreased after ~8 Ma, roughly parallel to the PWetQ variations (Fig. 4d; Peng et al., 2016). The chemical index of alteration (CIA) records, a widely used proxy for reconstruction of EASM, of the Sites 1146 and 1148 from the SCS show a gradual decrease trend from ~17–6 Ma, indicating the EASM intensity gradually weakened during the Miocene (Fig. 4c; Wan et al., 2010; Clift et al., 2014, Clift et al., 2008). However, the newest study proposes that the CIA is mainly controlled by temperature at million-year timescales (Ren et al., 2020), implying that CIA cannot be used as a precipitation proxy, which may explain some differences observed with our reconstruction.

The pedogenic carbon and oxygen isotope ($\delta^{13}C_{pedo}$ and $\delta^{18}O_{pedo}$) records from the nearby ZL core (Fig. 1b) show similarities with our records prior to 9.5 Ma: high values during the period of ~17–13.6 Ma and lower values between ~13.6 and 9.5 Ma (Fig. 4f; Dong et al., 2018). The most widely used magnetic parameter - frequency-dependent susceptibility (χ_{fd}) records of the QA section and ZL drilling core from the same basin (Fig. 1b) show similar variations to the PWetQ results: high values between ~17 Ma and ~ 13.5 Ma, decreased values between ~13.5 Ma and ~ 10 Ma, slightly increased values between ~10 Ma and ~ 8.7 Ma, low values between ~8.7 Ma and 7.4 Ma, and increased sharply values between ~7.4 Ma and 6.1 Ma (Fig. 4e and g; Hao et al., 2008, 2009). However, the long-term trend of these two records prior to ~8 Ma is different: the PWetQ records show a gradually decreasing trend and the χ_{fd} records a fluctuating pattern (Fig. 4a, e and g). Recently, another magnetic parameter - χ_{fd}/HIRM (hard isothermal remanence magnetization) has been used to reconstruct the Neogene EASM in the western Qaidam Basin (Nie et al., 2017, 2020; Ren et al., 2020). Their records indicate that most of the intensified EASM periods are corresponding with our records, e.g. the intervals of ~17–14 Ma, ~10–8.7 Ma and ~ 7.4–6 Ma, but the general trend is different from our records prior to ~8 Ma, (Fig. 4h; Ren et al., 2020; Nie et al., 2020). Therefore, the overall trends of the PWetQ, χ_{fd} and χ_{fd}/HIRM records prior to ~8 Ma are different from each other in long-term evolution (Fig. 4a, e and h).

5.2. Possible drive(s) for the Miocene EASM evolution

Our quantitative record suggests a relatively strong Miocene EASM occurred during the period of ~17–14.6 Ma. This period, corresponds to the warmest period of the Neogene - Middle Miocene Climatic Optimum (MMCO) recorded by the deep-sea oxygen isotopes (Zachos et al., 2001), the interval with the highest atmospheric CO_2 concentrations (Cui et al., 2020), the relatively stable tectonic activity of TP and lower NE TP relief during the Miocene (Li et al., 2014;Hui et al., 2018; Zhang et al., 2013). The strengthening of the EASM during the MMCO has been well recorded by fossils and other inorganic proxies in many areas of Asia (Miao et al., 2016 and references therein; Zhao et al., 2020a, Zhao et al., 2017; Nie et al., 2020; Deng, 2016; Dong et al., 2018). For example, a large number of mammals adapted to the warm and wet typical of the monsoon regions appeared in northern China during the MMCO, such as *Platybelodon*, *Pliopithecus*, beavers, *Anchitherium*, *Chalicotherium*, *Kubanochoerus* and *Palaeotragus*, implying an intense EASM at that time (Deng, 2016). Previous geological records also indicate that the strong EASM intensity period is corresponding to the higher CO_2 interval during the Cenozoic (Ren et al., 2020; Lu et al., 2013), which is further confirmed by our quantitative records.

Many studies have proved that the phased uplift of TP can result in strong EASM intensity (Ruddiman and Kutzbach, 1989; An et al., 2001; Ren et al., 2020; Shi et al., 1999; Tang et al., 2013). However, in our records the strongest EASM period occurred during the lower TP elevation interval (Fig. 5a, f and g; Li et al., 2014; Li et al., 2015; Hui

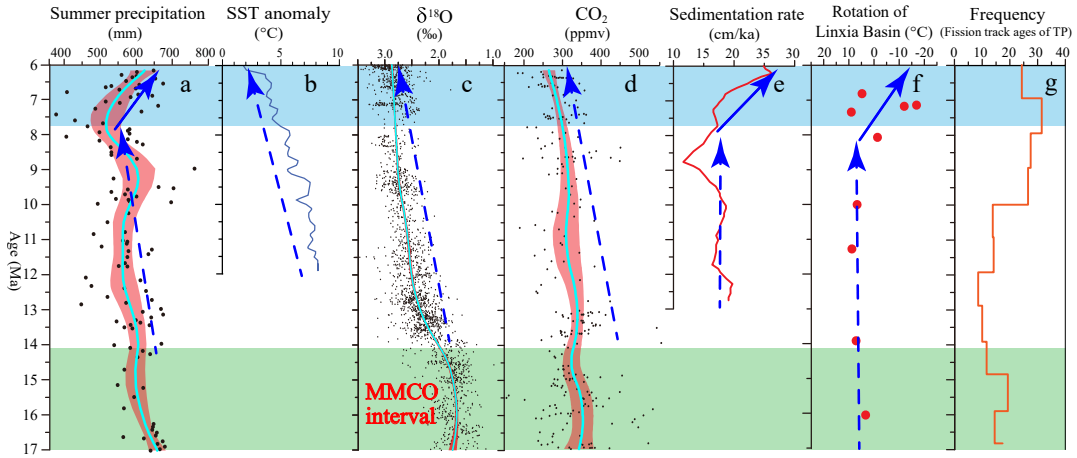

Fig. 5. EASM variations in the northern China and comparison with marine and global records. The blue lines in the summer precipitation, $\delta^{18}O$ and CO_2 panels represent the trends estimated using linear LOESS smoothing, the red envelopes represent the 2δ (standard deviation) uncertainty. The blue dashed line with arrow shows the general trend of tectonic rotation of the Linxia Basin on the northeastern TP, the blue solid lines with arrows highlight the strengthening of EASM and uplift of the northeastern TP, and the black solid lines with arrows highlight the climatic cooling period. The light green and cyan bans highlight the middle Miocene climate optimum (MMCO) and the strengthening EASM periods with associated driving force during late Miocene, respectively. (a) Summer precipitation records from the studied YW section in Tianshui Basin. (b) Sea surface temperature (SST) anomalies of North Hemisphere 30°–50°, obtained by subtracting modern SST at this latitude (Herbert et al., 2016). (c) Benthic oxygen isotope record (Zachos et al., 2001). (d) Miocene CO_2 records based on C_3 plant remains (Cui et al., 2020). (e) Average sedimentation rate records of the Hexi, Qaidam and Guide Basins on the northeastern TP (Licht et al., 2014). (f) Tectonic rotation records of the Linxia Basin on the northeastern TP (Fang et al., 2003; Licht et al., 2014). (g) Frequency histogram of apatite fission track ages from both the south and north TP (Zhang et al., 2013). (For interpretation of the references to colour in this figure legend, the reader is referred to the web version of this article.)

et al., 2018; Zhang et al., 2013). Therefore, the period of global warmth MMCO, probably resulting from elevated CO_2 levels (greenhouse gas; Kürschner et al., 2008; Foster et al., 2012) - should be the first-order driving force for the strongest EASM period during ~17–13.6 Ma. Our results support climate model simulations that stronger EASM precipitation occurred during warm periods, since the higher temperature and enhanced greenhouse conditions could increase the content of water vapor held in the atmosphere and reinforce the hydrological cycle, which can partly counterbalance the negative impact of lower Tibetan elevation on summer precipitation (Licht et al., 2014). Between ~13.6 and ~ 7.6 Ma, the EASM exhibited a gradual weakening trend, which is consistent with the gradual cooling of the global climate possibly resulting from reducing CO_2 that caused the expansion of the eastern Antarctic ice sheet (EAIS) (Fig. 5a, b, c and d; Foster et al., 2012; Herbert et al., 2016; Zachos et al., 2001; Cui et al., 2020).

The weakening of the EASM in a cooler period was also recorded by the quantitative reconstruction of EASM based on the phytoliths records from the Weihe Basin of North China (Fig. 1a; Wang et al., 2019). Therefore, we propose that the global cooling is main driver of the weakening of the EASM intensity during the period of ~13.6–7.4 Ma indicated by our quantitative reconstruction results. Cooler temperature, means a reduction of the water vapor held in the atmosphere, which can provide additional cooling through the reduced greenhouse effect (water vapor is a type of greenhouse gas), and with this positive feedback, further reduces EASM (Ruddiman, 2002). It should be noted that an intensified EASM interval occurred between ~10 Ma and 8.7 Ma against the background of EASM weakening, which is also recorded by the magnetic parameter of HTTL section in the Qaidam Basin (Fig. 1a; Ren et al., 2020). Its cause needs to be further investigated in the future.

After ~7.6 Ma, the EASM in our quantitative reconstruction increased significantly, at the same time, the global temperature and CO_2 continually decreased (Fig. 5a, b, c and d; Zachos et al., 2001; Cui et al., 2020), implying a decoupling of temperature and precipitation. Evidence of sedimentology, palaeomagnetism and thermochronology demonstrate that an intense uplift of the northeastern TP occurred during the Late Miocene (Li et al., 2014; Fang et al., 2007; Wang et al., 2011; Craddock et al., 2011; Xu et al., 2018). For example, the average sedimentation rate in Hexi, Qaidam and Guide Basins from northeastern TP rapidly increased since ~8 Ma, nearly doubled at ~6 Ma (Fig. 5e;Li et al., 2014); the palaeomagnetic declinations records from the nearby Linxia Basin indicate a clockwise rotation pattern beginning rapidly after ~8 Ma (Fig. 5f; Fang et al., 2003;Li et al., 2014). Furthermore, the analysis of apatite fission track ages from the whole TP indicates that both the south and north of TP further uplifted at ~8 Ma (Fig. 5g; Zhang et al., 2013). Therefore, we suggest that the increased EASM intensity after ~7.4 Ma in our records may have been caused by the uplift of the TP during the late Miocene through strengthening the thermal contrast and pressure gradient between land and sea, as simulated by climate models (An et al., 2001; Kutzbach et al., 1989; Wu et al., 2012; Farnsworth et al., 2019). In summary, our quantitative records of EASM demonstrate that both the global temperature and regional and/or local palaeogegraphy (uplift of TP) variations play important roles in regulating the Miocene EASM evolution on tectonic time scales.

6. Conclusion

Based on pollen floras and using the Bayesian approach CREST, this study presents a new and quantitative record of EASM precipitation during the Miocene, which demonstrates the potential of this Bayesian approach to reconstruct climate changes on tectonic time scales in northern China. The reconstruction of PWetQ shows that the Miocene EASM can be divided into three periods: the strongest and relative stable period of ~17.1–13.6 Ma, a relatively strong and gradual decreasing period between ~13.6 and 7.4 Ma and a period of sharply increasing precipitation between ~7.4 and 6.1 Ma. Moreover, the increasing standard deviation for each interval indicates the variation amplitude of EASM stepwise increased with time. Comparison of our reconstructions of summer precipitation and other proxy records from the region reveals that the staged decrease of EASM during the period of ~17.1–7.4 Ma was mainly a response to the global temperature variations, whereas the significant increase period of ~7.4–6.1 Ma was mainly related to the uplift of TP during the late Miocene. Thus, our new record supports the climate model simulations that both the global temperature and palaeogeography play important roles in regulating the long-term evolution of EASM.

Declaration of Competing Interest

The authors declare that they have no known competing financial interests or personal relationships that could have appeared to influence the work reported in this paper.

Acknowledgement

This work was co-supported by the National Natural Sciences Foundation of China (Grant Nos. 41877445 and 41771209) and the State Program of the National Natural Sciences Foundation of China (Grant No. 41330745). Manuel Chevalier was supported by the German Federal Ministry of Education and Research (BMBF) as a Research for Sustainability initiative (FONA; https://www.fona.de/en, last access: 25 September 2020) through the PalMod Phase II project (grant no. FKZ: 01LP1926D).Special thanks to Editor Howard Falcon-Lang and four anonymous reviewers for their constructive suggestions and comments on this paper.

Appendix A. Supplementary data

Supplementary data to this article can be found online at https://doi.org/10.1016/j.palaeo.2021.110609.

References

Alonso-Zarza, A.M., Zhao, Z., Song, C.H., Li, J.J., Zhang, J., Martín-Pérez, A., Martín-García, R., Wang, X.X., Zhang, Y., Zhang, M.H., 2009. Mudflat/distal fan and shallow lake sedimentation (upper Vallesian-Turolian) in the Tianshui Basin, Central China: evidence against the late Miocene eolian loess. Sediment. Geol. 222, 42–51. https://doi.org/10.1016/j.sedgeo.2009.03.010.

An, Z.S., Kutzbach, J.E., Prell, W.L., Porter, S.C., 2001. Evolution of Asian monsoons and phased uplift of the Himalaya-Tibetan plateau since late Miocene times. Nature 411, 62–66. https://doi.org/10.1038/35075035.

Ao, H., Roberts, P., Dekkers, A.J., XiaodongLiu, M., Rohling, J., Shi, E. Zhengguo, An, Zhisheng, Zhao, Xiang, 2016. Late Miocene-Pliocene Asian monsoon intensification linked to Antarctic ice-sheet growth. Earth Planet. Sci. Lett. 444, 75–87. https://doi.org/10.1016/j.epsl.2016.1003.1028.

Cande, S.C., Kent, D.V., 1995. Revised calibration of the Geomagnetic Polarity Timescale for the late Cretaceous and Cenozoic. J. Geophys. Res. 100, 6093–6095. https://doi.org/10.1594/PANGAEA.708128.

Chen, F., Xu, Q., Chen, J., Birks, H.J.B., Liu, J., Zhang, S., Jin, L., An, C., Telford, R.J., Cao, X., Wang, Z., Zhang, X., Selvaraj, K., Lu, H., Li, Y., Zheng, Z., Wang, H., Zhou, A., Dong, G., Zhang, J., Huang, X., Bloemendal, J., Rao, Z., 2015. East Asian summer monsoon precipitation variability since the last deglaciation. Sci. Rep. 5 https://doi.org/10.1038/srep11186.

Chevalier, M., 2019. Enabling possibilities to quantify past climate from fossil assemblages at a global scale. Glob. Planet. Chang. 175, 27–35. https://doi.org/10.1016/j.gloplacha.2019.1001.1016.

Chevalier, M., Cheddadi, R., Chase, B.M., 2014. CREST (climate REconstruction SofTware): a probability density function (PDF)–based quantitative climate reconstruction method. Clim. Past 10, 2081–2098. https://doi.org/10.5194/cp-10-2081-2014.

Chevalier, M., Chase, B.M., Quick, L.J., Dupont, L.M., Johnson, T.C., 2020. Temperature change in subtropical southeastern Africa during the past 790,000 yr. Geology. https://doi.org/10.1130/G47841.47841.

Clift, P.D., 2020. Asian monsoon dynamics and sediment transport in SE. Asia J. Asian Earth Sci. 195, 1–11. https://doi.org/10.1016/j.jseaes.2020.104352.

Clift, P.D., Plumb, R.A., 2008. The Asian Monsoon: Causes, History and Effects. Cambridge University Press, Cambridge.

Clift, P.D., Hodges, K.V., Heslop, D., Hannigan, R., Long, H.V., Calves, G., 2008. Correlation of Himalayan exhumation rates and Asian monsoon intensity. Nat. Geosci. 1, 875–880. https://doi.org/10.1038/ngeo351.

Clift, P.D., Wan, S., Blusztajn, J., 2014. Reconstructing chemical weathering, physical erosion and monsoon intensity since 25 Ma in the northern South China Sea: a review of competing proxies. Earth-Sci. Rev. 130, 86–102, 110.1016/j.earscirev.2014.1001.1002.

Craddock, W., Kirby, E., Zhang, H., 2011. Late Miocene-Pliocene range growth in the interior of the northeastern Tibetan Plateau. Lithosphere 3, 420–438.

Cui, Y., Schubert, B.A., Jahren, A.H., 2020. A 23 m.y. record of low atmospheric CO_2. Geology 48 (9), 888–892. https://doi.org/10.1130/G47681.1.

Deng, T., 2016. Records and characteristics of the mammalian faunas of northern China in the Middle Miocene Climatic optimum. Quat. Sci. 36, 810–819 (in Chinese with English abstract).

Dong, J., Liu, Z., An, Z., Liu, W., Zhou, W., Qiang, X., Lu, F., 2018. Mid-Miocene C_4 expansion on the Chinese Loess Plateau under an enhanced Asian summer monsoon. Journal of Asian Earth Sciences 158, 153–159. https://doi.org/10.1016/j.jseaes.2018.1002.1014.

Fang, X.M., Garzione, C., Van der Voo, R., Li, J.J., Fan, M.J., 2003. Flexural subsidence by 29 Ma on the NE edge of Tibet from the magnetostratigraphy of Linxia Basin, China. Earth Planet. Sci. Lett. 210, 545–560.

Fang, X., Zhang, W., Meng, Q., Gao, J., Wang, X., King, J., Song, C., Dai, S., Miao, Y., 2007. High-resolution magnetostratigraphy of the Neogene Huaitoutala section in the eastern Qaidam Basin on the NE Tibetan Plateau, Qinghai Province, China and its implication on tectonic uplift of the NE Tibetan Plateau. Earth and Planetary Science Letters 258, 293–306. https://doi.org/10.1016/j.epsl.2007.1003.1042.

Farnsworth, A., Lunt, D.J., Robinson, S.A., Valdes, P.J., Roberts, W.H.G., Clift, P.D., Markwick, P., Su, T., Wrobel, N., Bragg, F., Kelland, S.-J., Pancost, R.D., 2019. Past East Asian monsoon evolution controlled by paleogeography, not CO_2. Sci. Adv. 5, eaax1697, 1610.1126/sciadv.aax1697.

Foster, G., Lear, C., Rae, J., 2012. The evolution of pCO_2, ice volume and climate during the middle Miocene. Earth Planet. Sci. Lett. 341-344, 243–254. https://doi.org/10.1016/j.epsl.2012.06.007.

Hao, Q., Oldfield, F., Bloemendal, J., Guo, Z., 2008. The magnetic properties of loess and paleosol samples from the Chinese Loess Plateau spanning the last 22 million years. Palaeogeogr. Palaeoclimatol. Palaeoecol. 260, 389–404. https://doi.org/10.1016/j.palaeo.2007.11.010.

Hao, Q., Oldfield, F., Bloemendal, J., Torrent, J., Guo, Z., 2009. The record of changing hematite and goethite accumulation over the past 22 Myr on the Chinese Loess Plateau from magnetic measurements and diffuse reflectance spectroscopy. J. Geophys. Res. 114, B12101 https://doi.org/10.1029/2009JB006604.

Herbert, T.D., Lawrence, K.T., Tzanova, A., Peterson, L.C., Caballero-Gill, R., Kelly, C.S., 2016. Late Miocene global cooling and the rise of modern ecosystems. Nat. Geosci. 9, 843–849, 810.1038/ngeo2813.

Hui, Z., Li, J., Xu, Q., Song, C., Zhang, J., Wu, F., Zhao, Z., 2011. Miocene vegetation and climatic changes reconstructed from a sporopollen record of the Tianshui Basin, NE Tibetan Plateau. Palaeogeogr. Palaeoclimatol. Palaeoecol. 308, 373–382. https://doi.org/10.1016/j.palaeo.2011.05.043.

Hui, Z., Li, X., Ma, Z., Xiao, L., Zhang, J., Chang, J., 2018. Miocene pollen assemblages from the Zeku Basin, northeastern Tibetan Plateau, and their palaeoecological and palaeoaltimetric implications. Palaeogeogr. Palaeoclimatol. Palaeoecol. 511, 419–432.

Hui, Z., Ran, M., Li, H., Liu, C., Guo, B., Zhang, J., Peng, T., Liu, D., Pan, Y., 2020. Early Pleistocene pollen record from the western Chinese loess plateau and its implications for the evolution of the east Asian summer monsoon. Sci. Total Environ. https://doi.org/10.1016/j.scitotenv.2020.143304.

Jiang, H.C., Ding, Z.L., 2008. A 20 Ma pollen record of East-Asian summer monsoon evolution from Guyuan,Ningxia, China. Palaeogeogr. Palaeoclimatol. Palaeoecol. 265, 30–38. https://doi.org/10.1016/j.palaeo.2008.1004.1016.

Jiang, H., Ding, Z., 2009. Spatial and temporal characteristics of Neogene palynoflora in China and its implication for the spread of steppe vegetation. J. Arid Environ. 73, 765–772, 710.1016/j.jaridenv.2009.1003.1011.

Juggins, S., Simpson, G.L., Telford, R.J., 2015. Taxon selection using statistical learning techniques to improve transfer function prediction. Holocene 25, 130–136.

Kürschner, W.M., Kvacek, Z., Dilcher, D.L., 2008. The impact of Miocene atmospheric carbon dioxide fluctuations on climate and the evolution of terrestrial ecosystems. Proc. Natl. Acad. Sci. U. S. A 105, 449–453. https://doi.org/10.1073/pnas.0708588105.

Kutzbach, J.E., Guetter, P.J., Ruddiman, W.F., Prell, W., 1989. The sensitivity of climate to late Cenozoic uplift in Southeast Asia and the American southwest: Numerical experiments. J. Geophys. Res. 94, 18,393–18,407. https://doi.org/10.1029/JD094iD15p18393.

Li, J., Fang, X., Song, C., Pan, B., Ma, Y., Yan, M., 2014. Late Miocene–Quaternary rapid stepwise uplift of the NE Tibetan Plateau and its effects on climatic and environmental changes. Quaternary Research 81, 400–423. https://doi.org/10.1016/j.yqres.2014.1001.1002.

Li, J., Feng, Z., Tang, L., 1988. Late Quaternary monsoon patterns on the loess plateau of China. Earth Surf. Process. Landf. 13, 125–135.

Li, J., Xu, Q., Cao, X., Pan, R., Ding, W., Lin, F., 2011. Two year's pollen influx and pollen vertical dispersion in the Coniferous and deciduous broad-leaved mixed forest of Changbai mountain. Quat. Sci. 31, 171–179 (in Chinese with English abstract).

Li, J., Zhou, S., Zhao, Z., Zhang, J., 2015. The Qingzang movement: the major uplift of the Qinghai-Tibetan Plateau. Sci. China Earth Sci. 58, 1–10.

Licht, A., Cappelle, M., Abels, H., Ladant, J., Trabucho-Alexandre, J., France-Lanord, C., Donnadieu, Y., Vandenberghe, J., Rigaudier, T., Lecuyer Jr., C., Terry, D., Adriaens, R., Boura, A., Guo, Z., Soe, A., Quade, J., Dupont-Nivet, G., Jaeger, J., 2014. Asian monsoons in a late Eocene greenhouse world. Nature 513, 501–506.

Liu, J., Li, J., Song, C., Yu, H., Peng, T., Hui, Z., Ye, X., 2016. Palynological evidence for late Miocene stepwise aridification on the northeastern Tibetan Plateau. Clim. Past 12, 1473–1484, 1410.5194/cp-1412-1473-2016.

Lu, H., Yi, S., Liu, Z., Mason, J.A., Jiang, D., Cheng, J., Stevens, T., Xu, Z., Zhang, E., Jin, L., Zhang, Z., Guo, Z., Wang, Y., Otto-Bliesner, B., 2013. Variation of East Asian monsoon precipitation during the past 21 k.y. and potential CO_2 forcing. Geology 41, 1023–1026, 1010.1130/G34488.34481.

Lu, F., Ma, C., Zhu, C., Lu, H., Zhang, X., Huang, K., Guo, T., Li, K., Li, L., Li, B., Zhang, W., 2019. Variability of East Asian summer monsoon precipitation during the Holocene and possible forcing mechanisms. Clim. Dyn. https://doi.org/10.1007/s00382-018-4175-6.

Ma, Y.Z., Fang, X.M., Li, J.J., Wu, F.L., Zhang, J., 2005. The vegetation and climate change during Neocene and Early Quaternary in Jiuxi Basin, China. Science in China Ser. D Earth Sciences 5, 676–688. https://doi.org/10.1360/1303yd0110.

Ma, Y.Z., Li, J.J., Fang, X.M., 1998. Pollen assemblage in 30.6-5.0Ma redbeds of Linxia region and climate evolution. Chinese Science Bulletin 43, 301–304.

Miao, Y., Song, C., Fang, X., Meng, Q., Zhang, P., Wu, F., Yan, X., 2016. Late Cenozoic genus *Fupingopollenites* development and its implications for the Asian summer monsoon evolution. Gondwana Res. 29, 320–333, 310.1016/j.gr.2014.1012.1007.

Miao, Y., Warny, S., Clift, P.D., Liu, C., Gregory, M., 2017. Evidence of continuous Asian summer monsoon weakening as a response to global cooling over the last 8 Ma. Gondwana Res. 52, 48–58. https://doi.org/10.1016/j.gr.2017.1009.1003.

Nie, J.S., Garzione, C.N., Su, Q.D., Liu, Q., Zhang, R., Heslop, D., Necula, C., Zhang, S., Song, Y., Luo, Z., 2017. Dominant 100,000-year precipitation cyclicity in a late Miocene lake from Northeast Tibet. Sci. Adv. 3, e1600762 https://doi.org/10.1126/sciadv.1600762.

Nie, J., Ren, X., Saylor, J.E., Su, Q., Horton, B.K., Bush, M.A., Chen, W., Pfaff, K., 2020. Magnetic polarity stratigraphy, provenance, and paleoclimate analysis of Cenozoic strata in the Qaidam Basin, NE Tibetan Plateau. Geol. Soc. Am. Bull. 132, 310–320. https://doi.org/10.1130/B35175.1.

Peng, T., Li, J., Song, C., Guo, B., Liu, J., Zhao, Z., Zhang, J., 2016. An integrated biomarker perspective on Neogene Quaternary climatic evolution in NE Tibetan Plateau: implications for the Asian aridification. Quat. Int. 399, 174–182. https://doi.org/10.1016/j.quaint.2015.04.020.

Piao, J., Chen, W., Wang, L., Pausata, F.S.R., Zhang, Q., 2020. Northward extension of the East Asian summer monsoon during the mid-Holocene. Glob. Planet. Chang. 184 (103046) https://doi.org/10.1016/j.gloplacha.2019.103046.

Qiang, X., An, Z., Song, Y., Chang, H., Sun, Y., Liu, W., Ao, H., Dong, J., Fu, C., Wu, F., Lu, F., Cai, Y., Zhou, W., Cao, J., Xu, X., Ai, L., 2011. New eolian red clay sequence on the western Chinese Loess Plateau linked to onset of Asian desertification about 25 Ma ago. Science China Earth Sciences 54 (1), 136–141. https://doi.org/10.1007/s11430-11010-14126-11435.

Ren, X., Nie, J., Saylor, J.E., Wang, X., Liu, F., Horton, B.K., 2020. Temperature control on silicate weathering intensity and evolution of the Neogene East Asian summer monsoon. Geophys. Res. Lett. 47 https://doi.org/10.1029/2020GL088808.

Ruddiman, W.F., 2002. Earth's Climate: Past and Future. W.H. Freman and Company, New York.

Ruddiman, W.F., Kutzbach, J.E., 1989. Forcing of late Cenozoic northern hemisphere climate by plateau uplift in southern Asia and the American West. J. Geophys. Res. 94, 18409–18427.

Sun, Y., Ma, L., Bloemendal, J., Clemens, S., Qiang, X., An, Z., 2015. Miocene climate change on the Chinese Loess Plateau: Possible links to the growth of the northern Tibetan Plateau and global cooling. Geochem. Geophys. Geosyst. 16, 2097–2108, 2010.1002/2015GC005750.

Sun, X., Wang, P., 2005. How old is the Asian monsoon system?—Palaeobotanical records from China. Palaeogeography, Palaeoclimatology, Palaeoecology 222, 181–222. https://doi.org/10.1016/j.palaeo.2005.1003.1005.

Tang, H., Micheels, A., Eronen, J.T., Ahrens, B., Fortelius, M., 2013. Asynchronous responses of East Asian and Indian summer monsoons to mountain uplift shown by regional climate modelling experiments. Clim. Dyn. 40, 1531–1549, 1510.1007/s00382-00012-01603-x.

Wan, S., Clift, P.D., Li, A., Li, T., Yin, X., 2010. Geochemical records in the South China Sea: implications for East Asian summer monsoon evolution over the last 20. In: Ma Clift, P.D., Tada, R., Zheng, H. (Eds.), Monsoon Evolution and Tectonics–Climate Linkage in Asia, 342. Geol. Soc. Lond., Spec. Publ., pp. 245–263

Wang, X., Li, J., Song, C., Zattin, M., Zhao, Z., Zhang, J., Zhang, Y., He, K., 2011. Late Cenozoic orogenic history of Western Qinling inferred from sedimentation of Tianshui basin, northeastern margin of Tibetan Plateau. Int. J. Earth Sci. (Geol Rundsch). https://doi.org/10.1007/s00531-011-0724-5.

Wang, H., Lu, H., Zhao, L., Zhang, H., Lei, F., Wang, Y., 2019. Asian monsoon rainfall variation during the Pliocene forced by global temperature change. Nat. Commun. 10, 5272, 5210.1038/s41467-41019-13338-41464.

Wang, Y., Lu, H., Wang, K., Wang, Y., Li, Y., Clemens, S., Lv, H., Huang, Z., Wang, H., Hu, X., Lu, F., Zhang, H., 2020. Combined high- and low-latitude forcing of East Asian monsoon precipitation variability in the Pliocene warm period. Sci. Adv. 6, eabc2414.

Webster, P.J., Magana, V.O., Palmer, T.N., Shukla, J., Tomas, R.A., Yanai, M., Yasunari, T., 1998. Monsoons: Processes, predictability, and the prospects for prediction. J. Geophys. Res. 103, 14451–14510.

Wei, G., Li, X.-H., Liu, Y., Shao, L., Liang, X., 2006. Geochemical record of chemical weathering and monsoon climate change since the early Miocene in the South China Sea. Paleoceanography 21, PA4214. https://doi.org/10.1029/2006PA001300.

Wu, G., Liu, Y., He, B., Bao, Q., Duan, A., Jin, F.-F., 2012. Thermal Controls on the Asian summer monsoon. Sci. Rep. 2, 404, 410.1038/srep00404.

Xu, Q., Li, Y., Yang, X., Chen, H., Lv, X., 2005. A study of some typical pollen types taphonomy and relationships with vegetation in the northeast of Qinghai-Tibet Plateau. Adv. Earth Science 20, 89–98 (in Chinese with English abstract).

Xu, Y., Zhang, K., Yang, Y., Wang, G., Luo, M., Ji, J., Song, B., 2018. Neogene evolution of the north-eastern Tibetan Plateau based on sedimentary, paleoclimatic and tectonic evidence. Palaeogeogr. Palaeoclimatol.Palaeoecol. 512, 33–45.

Zachos, J., Pagani, M., Sloan, L., Thomas, E., Billups, K., 2001. Trends, Rhythms, and Aberrations in Global climate 65 Ma to present. Science 292, 686–693.

Zhang, K., Wang, G., Hong, H., Xu, Y., Wang, A., Cao, K., Luo, M., Ji, J., Xiao, G., Lin, X., 2013. The study of the Cenozoic uplift in the Tibetan Plateau: a review. Geol. Bull. China 32, 1–18 (in Chinese with English abstract).

Zhang, R., Zhang, Z., Jiang, D., 2018. Global Cooling Contributed to the Establishment of a Modern-Like East Asian Monsoon Climate by the Early Miocene. Geophys. Res. Lett. 45, 11941–11948, 11910.11029/12018GL079930.

Zhao, H., Sun, Y., Qiang, X., 2017. Iron oxide characteristics of mid-Miocene Red Clay deposits on the western Chinese Loess Plateau and their paleoclimatic implications. Palaeogeogr. Palaeoclimatol. Palaeoecol. 468, 162–172.

Zhao, H., Qiang, X., Xu, X., Sun, Y., 2020a. Iron oxide characteristics of the Chinese loess-red clay sequences and their implications for the evolution of the East Asian summer monsoon since the late Oligocene. Palaeogeogr. Palaeoclimatol. Palaeoecol. 534, 109604, 109610.101016/j.palaeo.102020.109604.

Zhao, L., Lu, H., Wang, H., Meadows, M., Ma, C., Tang, L., Lei, F., Zhang, H., 2020b. Vegetation dynamics in response to evolution of the Asian Monsoon in a warm world: pollen evidence from the Weihe Basin, Central China. Glob. Planet. Chang. 193, 103269, 103210.101016/j.gloplacha.102020.103269.